

Exploring the benefits of vertically staggered wind farms: Understanding the power generation mechanisms of turbines operating at different scales

Tanmoy Chatterjee^{ID} | Yulia Peet

School for Engineering of Matter, Transport, and Energy (SEMTE), Arizona State University, Tempe, Arizona

Correspondence

Tanmoy Chatterjee, School for Engineering of Matter, Transport and Energy (SEMTE), Arizona State University, 501 E. Tyler Mall, Tempe, AZ 85287.

Email: tchatt3@asu.edu

Funding information

National Science Foundation USA,
Grant/Award Number: NSF-CBET 13358568

Abstract

Wind farms are known to modulate large scale structures in and around the wake regions of the turbines. The potential benefits of placing small hub height, small rotor turbines in between the large turbines in a wind farm to take advantage of such modulated large-scale eddies are explored using large eddy simulation (LES). The study has been carried out in an infinite wind farm framework invoking an asymptotic limit, and the wind turbines are modeled using an actuator line model. The vertically staggered wind turbine arrangements that are studied in the present work consist of rows of large wind turbines, with rows of smaller wind turbines (ie, smaller rotor size and shorter hub height) placed in between the rows of large turbines. The influence of the hub height of the small turbines, in particular, how it affects the interactions between the large and small turbines and consequently their power, along with the multiscale dynamics involved, has been assessed in the current study. It was found that, in the multiscale layouts, the small turbines at lower hub heights operate more efficiently than their homogeneous single-scale counterparts. In contrast, the small turbines with higher hub heights incur a loss of power compared with the corresponding single-scale arrangements.

KEYWORDS

infinite wind farms, large eddy simulations, vertically staggered, wind power

1 | INTRODUCTION

Wind farms featuring large arrays of horizontal axis wind turbines (HAWTs) have become popular since the last two decades as a viable method of extracting wind energy from the atmospheric boundary layer (ABL) and converting it into electric power.^{1–3} The atmospheric turbulent flow intercepted by the turbines produces a low-velocity region downstream of the turbines known as wakes. In large wind farms composing of many arrays of wind turbines, the wakes from the previous rows of wind turbines impinge on the turbines at subsequent rows, reducing the power and increasing the structural loads of those turbines. Horizontal staggering of wind turbines is a popular way of optimizing the layout of wind farms^{4–7} to reduce wake impingements, where the wind turbine positions in two consecutive rows are offset from each other. Compared with horizontal staggering, vertical staggering of wind farms, ie, offsetting the wind turbine hub heights, is relatively less explored. A few experimental studies were concerned with the situation where, in a model wind farm, every second row of turbines was replaced with the turbines of smaller hub heights, while leaving the rotor diameters intact, or lowering it slightly in proportion with the hub height. Chamorro et al⁸ studied an experimental model wind farm where HAWTs of two different rotor sizes and hub heights were alternated and demonstrated that distinctive flow features not present in a single-size (homogeneous) wind farm were observed that led to a reduced level of turbulence around the wind turbine rotors and more homogeneous flow through the wake mixing. Although potential benefits of reduced turbulence levels on turbine loading were implied, the effects on power were not directly measured. Vested et al⁹ documented experiments with a model of a vertically staggered wind farm featuring HAWTs of two different hub heights but identical rotor sizes and reported 25% increase in the power of shorter wind turbines operating behind the taller ones, as compared with the base configuration with short wind turbines only. In these studies, the differences between the turbine sizes (hub heights and rotor diameters), and consequently, their power capacities, have not exceeded 30% to 40%, which makes

wind turbines operate essentially on the same scale in terms of power production. Several recent studies^{10–12} have explored the effect of hub height optimization in vertically staggered wind farms utilizing a semianalytical wake model called PARK model.¹³ Vasel-Be-Hagh and Archer¹⁴ used a similar optimization framework and validated their optimized layout with large eddy simulations. These works have shown the potential power benefits of vertically staggered configurations with the maximum benefit obtainable at offshore locations with tight spacing between the turbines. The aforementioned studies have focused on a hub height being a primary optimization variable, while the rotor diameters were kept fixed for all the turbines.

In this paper, we aim to further explore the idea of vertical staggering of the turbines and introduce the concept of a multiscale wind farm, where, in addition to wind turbines operating at a larger scale of power production, the turbines with significantly smaller sizes (in terms of both rotor sizes and hub heights) and thus power capacities are added to an existing large-scale wind farm configuration.

The concept is slightly different from the same-scale variable-height wind farms, in a sense that a nearly optimum layout for the wind turbines operated at large scales (that by itself can have variable hub heights for best performance) is enriched by adding more small turbines (rather than replacing the existing large turbines), and an effective increase of the wind farm capacity beyond the baseline level is expected. The turbines in such multiscale designs have a potential to influence each other both through a direct interference via wake mixing, and also through a global modulation of the turbulent boundary layer and the energetics of large-scale coherent structures. From a perspective of efficiency, for a practical multiscale wind farm design, one would expect that these interactions are at least not destructive; that is, the performance of the turbines at each scale is not negatively influenced by the presence of the turbines at the other scale. Another added benefit of a multiscale wind farm as compared with a combination of separate single-scale homogeneous arrangements is the reduced cost of the terrain and electrical power lines. Along the lines of such a vertically staggered, multiscale, wind farm design, Xie et al¹⁵ in their recent study performed large eddy simulations of a collocated wind farm where 20 small vertical axis wind turbines (VAWT; with 100 times lower capacity and almost 6 times lower hub heights) were placed around each large HAWT turbine. Xie et al¹⁵ documented 32% increase in the overall wind farm power generation, mostly coming from high density (ratio of a number of small to large turbines of 20 to 1) of the added VAWTs. Although the increase in power levels extracted by the large turbines (by about 10%) was demonstrated as well, due to a faster wake recovery from enhanced turbulence introduced by the small turbines, the same enhanced turbulence levels were also responsible for the increase in power fluctuations (variability), which has a negative effect on turbine fatigue loading. In the current paper, we aim to explore whether such a “multiscale wind farm” idea works for more conventional, HAWT-only, wind farm designs. Note that DuPont et al¹⁶ have recently performed an optimization study of a similar multiscale wind farm where both the hub heights and the rotor radii were optimized simultaneously in a wind farm layout. In this study, the hub heights were varied from 38 to 135 m and the rotor radii from 19 to 67 m; ie, the optimization variables were allowed to vary by as much as three times. The study, again, used the PARK model, and the distinction between the HAWT and VAWT turbines could not be made, since a very simplistic algebraic power model was used.

Our idea of a multiscale wind farm stems from our previous work^{17,18} that illustrated the presence of energetic and organized eddies originating around the wind turbine wakes and spreading below the rotor region, which were not seen in atmospheric flows without the wind turbines. Since large scale organizations have significant contribution to wind turbine power,^{6,19} one of the goals of the current work is to show that there is a potential of an efficient harvesting of these large-scale structures by smaller turbines that can also lead to a reduced power variability in these turbines. We also document that the choice of the hub heights for the small turbines influences the efficiency of the multiscale wind farm design. In this paper, large eddy simulations with an actuator line model for wind turbines are employed to study these effects. We note that wind turbine towers were not modeled in the current study. Although the current computations invoke the framework of asymptotically infinite wind farms through incorporation of periodic boundary conditions, we expect that the current findings can be qualitatively generalized to the finite wind farm situations, where the savings from the land cost make multiscale configurations especially enticing.

2 | COMPUTATIONAL SETUP

The computational domain composes of a periodic wind turbine array, with dimensions $21D_L \times 9D_L \times 3D_L$, where D_L is the diameter of the large turbine. The rows with small turbines of diameter, $D_S = 0.3D_L$, are placed mid-way between the rows with large turbines. In the current study, the diameter of the small turbines is kept fixed, while we consider two separate cases with different hub height of these small turbines in order to study the potential benefits of vertical staggering. In order to distinguish between the cases, we will call the small turbines placed at the smaller hub heights as “small,” small turbines placed at the higher hub heights as “intermediate,” while the turbines with large rotor sizes will be referred to as “large” (note that “small” and “intermediate” turbines have the same rotor size).

The dynamics and power of the large turbines in the vertically staggered arrangements containing large-small and large-intermediate turbines is compared against the baseline case composing of only the large turbines in a periodic arrangement. In an analogous way, the dynamics and power of the small/intermediate wind turbines in the multiscale (vertically staggered) arrangements are compared against the arrays consisting of only small/intermediate wind turbines at corresponding hub heights arranged in a periodic layout. Figure 1 illustrates the schematics of the computational setup for the investigated multiscale and single-scale periodic arrays. Unlike in previous variable-height wind farm studies involving HAWT turbines of comparable sizes and hub heights (within roughly 70% of each other),^{8,9} our current approach involves wind turbine dynamics at disparate length scales in such multiscale wind farm designs.

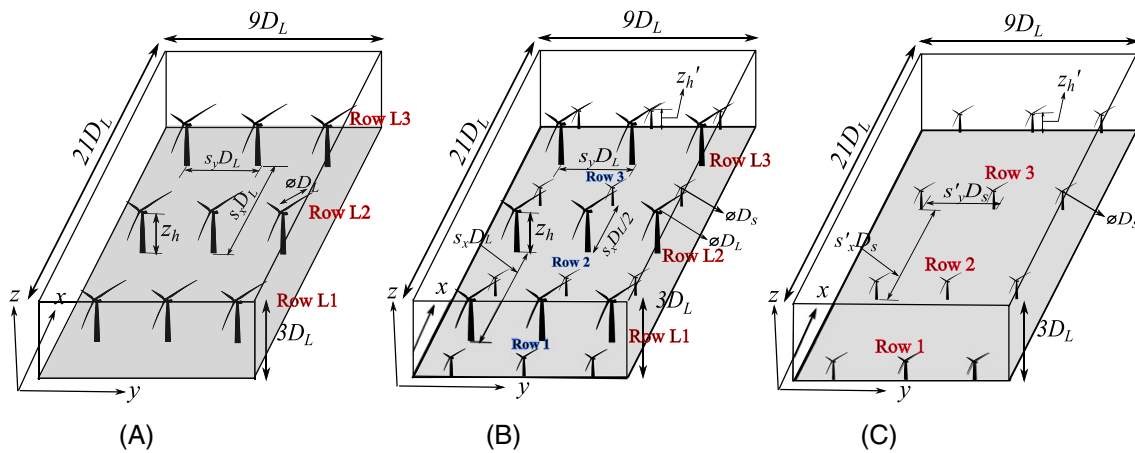


FIGURE 1 Schematic of the computational domain of A, baseline case L , with large turbines in a periodic arrangement; B, vertically staggered multiscale periodic wind farm of cases $L\xi^M$ with large + small/intermediate turbines ($\xi = S, I$); and C, small/intermediate turbines in periodic arrangements S, I . Interturbine distances, $s'_x D_s = s_x D_L$, $s'_y D_s = s_y D_L$. Rows for large turbines: $L1 - L3$. Rows for small/intermediate turbines: $1 - 3$. The last (fourth) row of the small/intermediate turbines in B and C is a repeated image of the first row due to periodicity and thus is not considered in the subsequent analysis [Colour figure can be viewed at wileyonlinelibrary.com]

TABLE 1 Geometric parameters and grid sizes of large and small turbines in multiscale and homogeneous/periodic wind farm arrangement^a

Case	N_{turb}	Δx_{turb}	Δy_{turb}	z_h	z'_h	D_s/D_L	$N_x^e \times N_y^e \times N_z^e$	N_{xyz}
L	$3 \times 3(L)$	$7D_L$	$3D_L$	D_L	–	–	$42 \times 30 \times 24$	1.05×10^7
S	$3 \times 3(S)$	$7D_L$	$3D_L$	–	$0.3D_L$	–	$36 \times 30 \times 24$	9.02×10^6
I	$3 \times 3(I)$	$7D_L$	$3D_L$	–	$0.6D_L$	–	$36 \times 30 \times 24$	9.02×10^6
LS^M	$3 \times 3(L) + 3 \times 3(S)$	$3.5D_L$	$3D_L$	D_L	$0.3D_L$	0.3	$48 \times 36 \times 32$	1.92×10^7
LI^M	$3 \times 3(L) + 3 \times 3(I)$	$3.5D_L$	$3D_L$	D_L	$0.6D_L$	0.3	$48 \times 36 \times 32$	1.92×10^7

^aThe scale of large turbines with respect to the ABL thickness is $D_L/H = 1/3$. L, S, I in brackets refer to the large, small and intermediate turbines. $N_{x,y,z}^e$, number of spectral elements in the x, y , and z direction; N_{xyz} is the total number of gridpoints.

All the simulations in this paper have been carried out using wall-modeled large eddy simulation in a neutrally stratified ABL framework in an open-source spectral element (SEM) research code Nek5000.²⁰ The simulation domain in Nek²¹ is subdivided into hexahedral elements, and within each element the variables, velocity and pressure, are expanded into a series of orthogonal Lagrange-Legendre interpolating polynomials. The number of grid points per element corresponds to $p + 1$ in each direction, where p is the order of the polynomial. The polynomial order $p = 7$ was used in all the simulations presented in the current paper. The computational framework involves periodic boundary conditions in the streamwise-spanwise direction, free-slip condition at the top, and stress boundary condition (wall model) at the bottom rough wall. The details of the Smagorinsky based subgrid scale model and shear-stress rough-wall boundary conditions in spectral elements used in our wall-modeled LES can be found in Chatterjee and Peet.^{22,23}

The following acronyms are used for the wind turbine arrangements: for single-scale arrangements containing large only turbines, L is used, while LS^M and LI^M refer to the multiscale arrangements of large-small and large-intermediate turbines, and S and I are used for small and intermediate only periodic arrangements. Additionally, to define the turbines within the layouts, we use non-italic symbols L, S , and I for large, small, and intermediate turbines, respectively, inside the single-scale layouts. To distinguish between the turbines in the single-scale and multiscale arrangements, for example, for large turbines, we use the acronyms L and L^M , respectively. Similar treatment is done for the small/intermediate turbines with using the superscript M to remind the readers about their location in the multiscale arrangements.

The details of the wind turbine array parameters for all the five simulated cases, eg, the hub heights ($z_h = D_L$ of the large turbines and $z'_h = 0.3D_L/0.6D_L$ of the small/intermediate turbines), the ratio of turbine diameters D_s/D_L (=0.3), the inter-turbine streamwise and spanwise distances, $\Delta x_{turb}, \Delta y_{turb}$, together with the number of spectral elements and grid points employed, are provided in Table 1. It must be noted that due to the difference in hub heights of the small and intermediate turbines, in the multiscale layout LS^M , the small turbines remain outside the wakes of the large turbines, while there is a 30% overlap in the area of the rotors of the large and intermediate turbines resulting in wake mixing in the layout LI^M . The scale of the large wind turbines with respect to the ABL thickness H is $D_L/H = 1/3$. We also define the nondimensional interturbine distances, s_x, s_y , for the large wind turbines, as $s_x = \Delta x_{turb}/D_L, s_y = \Delta y_{turb}/D_L$, and s'_x, s'_y , for the small/intermediate wind turbines, as $s'_x = \Delta x_{turb}/D_s, s'_y = \Delta y_{turb}/D_s$, which will be useful in the discussion to follow, and summarize them in Table 2.

TABLE 2 Nondimensional interturbine distances normalized with D_L for large turbines, and with D_S for small /intermediate turbines

Turbines	Streamwise distance	Spanwise distance
L, L^M	$s_x = 7$	$s_y = 3$
S, I, S^M, I^M	$s'_x = 23.1$	$s'_y = 9.9$

TABLE 3 The maximum, minimum, and the average grid sizes in the x , y , and z direction for the five simulation cases, L , S , I , LS^M , and LI^M ^a

Case	$\Delta_{x,\max}$	$\Delta_{x,\min}$	Δ_x	$\Delta_{y,\max}$	$\Delta_{y,\min}$	Δ_y	$\Delta_{z,\max}$	$\Delta_{z,\min}$	Δ_z
$L (: H)$	0.038 H	0.016 H	0.024 H	0.031 H	0.008 H	0.014 H	0.0067 H	0.0031 H	0.0060 H
$L (: D_L)$	0.115 D_L	0.05 D_L	0.072 D_L	0.095 D_L	0.024 D_L	0.042 D_L	0.020 D_L	0.009 D_L	0.018 D_L
$S (: H)$	0.04 H	0.006 H	0.028 H	0.032 H	0.0026 H	0.014 H	0.0067 H	0.001 H	0.0060 H
$S (: D_S)$	0.4 D_S	0.055 D_S	0.28 D_S	0.32 D_S	0.026 D_S	0.14 D_S	0.067 D_S	0.01 D_S	0.06 D_S
$I (: H)$	0.04 H	0.006 H	0.028 H	0.032 H	0.0026 H	0.014 H	0.0067 H	0.001 H	0.0060 H
$I (: D_S)$	0.4 D_S	0.055 D_S	0.28 D_S	0.32 D_S	0.026 D_S	0.14 D_S	0.067 D_S	0.01 D_S	0.06 D_S
$LS^M (: H)$	0.038 H	0.006 H	0.0206 H	0.031 H	0.0026 H	0.012 H	0.0067 H	0.0012 H	0.0045 H
$LS^M (: D_L)$	0.11 D_L	0.02 D_L	0.0625 D_L	0.095 D_L	0.008 D_L	0.036 D_L	0.02 D_L	0.0032 D_L	0.0135 D_L
$LS^M (: D_S)$	0.38 D_S	0.055 D_S	0.206 D_S	0.31 D_S	0.026 D_S	0.12 D_S	0.067 D_S	0.01 D_S	0.045 D_S
$LI^M (: H)$	0.038 H	0.006 H	0.0206 H	0.031 H	0.0026 H	0.012 H	0.008 H	0.0012 H	0.0045 H
$LI^M (: D_L)$	0.11 D_L	0.02 D_L	0.0625 D_L	0.095 D_L	0.008 D_L	0.036 D_L	0.026 D_L	0.0032 D_L	0.0135 D_L
$LI^M (: D_S)$	0.38 D_S	0.055 D_S	0.206 D_S	0.31 D_S	0.026 D_S	0.12 D_S	0.08 D_S	0.01 D_S	0.045 D_S

^aGrids are scaled with the domain height H and the rotor diameters D_L , D_S as appropriate.

2.1 | Actuator line model—grid design and blade parameters

The wind turbine blades are modeled using actuator lines^{22,24–26} in the spectral element formulation, emulating the rotation of the blades from the local lift and drag forces experienced by each blade “element” and projected as the body forces onto the neighboring grid points. Each actuator line was discretized using $N_a = 30$ uniformly sized blade elements (ie, per rotor radius).²⁴ In addition, a background SEM grid corresponding to neutral ABL²³ was refined to ensure a similar grid resolution of approximately 8×8 spectral elements, or 60×60 collocation points, in the rotor swept area in the yz plane. An additional refinement was done in the wake of the wind turbines to capture the helical vortices shed by the turbines.²⁴

Table 3 containing the maximum, minimum, and average grid sizes of the five cases, L , S , I , LS^M , LI^M used in the simulations has been provided for a reference. It is clear that in the yz plane of the turbine rotors and in the near wake, the grids scale with the *rotor diameter*, while away from the turbines, where ABL flow is dominant, the grids scale with the *domain height*. Considering the baseline grids S , I , the grid in the near-wake region of the rotors (approximately three rotor diameters) of case L manifests additional refinement in order to capture smaller spectral scales for future analysis. The overall grid resolution for all the cases was designed to capture spectral scales larger than rotor diameter D , which are the main contributors to the turbine power^{18,19} while keeping the near-turbine resolution adequate for capturing the effects of the rotating blades. Further, it can be understood that the multiscale cases require more elements in all three directions than the single-scale cases. In the xy direction, the element refinement occurs due to the presence of additional turbines compared with the single-scale layout and in the z direction, the refinement in multiscale cases is required due to a vertical staggering of the turbines.

To assess the validity of the vertical size of the domain in the simulations, the blockage ratio for all the five simulated cases is calculated in Table 4. The blockage ratio is computed as the ratio of the projected area of the turbine rotors in the lateral yz cross section to the total area of the yz cross section. For single-scale wind farms and a multiscale case LS^M , where there is no overlap between the turbine rotors in the frontal plane, the projected area is simply the sum of all the turbine discs in a row. For a multiscale layout LI^M , where an area of overlap exists between the large and intermediate turbine rotors in the frontal plane, the overlapping area is subtracted for the calculation of the blockage ratio. The overlapping area A_{ov} can be straightforwardly calculated using trigonometric identities.¹⁶ The blockage ratio for the cases involving only small and intermediate turbines is negligible, and the blockage ratio for the cases involving large turbines remain within 10%. Studies on blockage effects in wind tunnel experiments involving bluff bodies^{27,28} have indicated that the results are not significantly affected when the blockage ratio is less than 10%. Recent studies on the blockage effects involving HAWTs in wind tunnel experiments and LES simulations^{29,30} concluded that the blockage effects increase with the increase in the tip speed ratio along with the blockage ratio, however confirmed that generally no blockage corrections are necessary when the blockage ratio is less than 10% and the tip speed ratio is below its optimal value, both of which conditions are satisfied in the current study. Another important difference considering the blockage ratio effects in wind-tunnel experiments versus current simulations is that the top boundary in wind tunnel tests is a wall that represents more significant effects of the flow confinement, than a top symmetry boundary condition in the current simulations. The top symmetry boundary condition acts as a restriction of the mass transfer³¹ and

TABLE 4 Blockage ratio of five different single-scale and multiscale layouts used for LES simulations^a

Case	Analytical formula	Blockage ratio (%)
L	$(3 \times \pi D_L^2 / 4) / (L_y L_z)$	8.6%
S	$(3 \times \pi D_S^2 / 4) / (L_y L_z)$	0.79%
I	$(3 \times \pi D_S^2 / 4) / (L_y L_z)$	0.79%
LS ^M	$(3 \times (\pi D_L^2 / 4 + \pi D_S^2 / 4)) / (L_y L_z)$	9.43%
LI ^M	$(3 \times (\pi D_L^2 / 4 + \pi D_S^2 / 4 - A_{ov})) / (L_y L_z)$	8.72%

^a $L_y = 9D_L$, $L_z = 3D_L$. Overlapping area of the rotors in Case LI^M, $A_{ov} \approx 7D_S^2$

in fact is similar to a physical effect of the capping inversion layer in neutral ABL flows.³² Subsequently, the current simulation setup can also be thought to behave analogously to the situation when the large turbines are operating close to the capping inversion layer.

The turbine geometry for the small and intermediate wind turbines corresponds to the specifications of a 2 MW three-bladed Tjæreborg turbine.^{24,33} This choice has been made due to a close match between the specified rotor diameter $D_S = 0.1H$ of the small and intermediate turbines and the Tjæreborg rotor diameter of 61.1 m, when a typical thickness of a neutral ABL is assumed,³⁴ and a public availability of the data. The chord length and the pitch angle in Tjæreborg turbine vary linearly with radius as specified in a previous study.³³ The airfoil series employed are NACA 44xx airfoils varying between the thickness of 24% at the hub and 12% at the tip. The airfoil data ($C_l(\alpha)$, $C_d(\alpha)$) is taken from wind tunnel measurements performed on NACA airfoils at a chord Reynolds number $Re = 6 \times 10^6$.³³ The geometry for the large wind turbines is also based on a three-bladed turbine and is scaled up from the baseline geometry proportionally to the rotor diameter, while the same airfoil series and airfoil data are used to maintain a scale similarity between the turbines for a consistent performance comparison.³⁵

In the actuator line model, the local lift ($L_{i,k}$) and drag ($D_{i,k}$) forces experienced by each discrete blade element i of each turbine k are calculated as

$$\begin{aligned} L_{i,k} &= \frac{1}{2} C_l(\alpha_{i,k}) \rho V_{rel,i,k}^2 c_{i,k} w_{d,k}, \\ D_{i,k} &= \frac{1}{2} C_d(\alpha_{i,k}) \rho V_{rel,i,k}^2 c_{i,k} w_{d,k}, \end{aligned} \quad (1)$$

where $c_{i,k}$ is the chord length of the corresponding airfoil at each blade element location i of the turbine k and $w_{d,k}$ is the width of the actuator line elements, which is kept constant at each actuator line and thus only varies between the turbines and not the blade element locations. $V_{rel,i,k}$ is the local velocity magnitude relative to the rotating blade element and is computed from the velocity triangle for the rotating blade (see also Figure 2) as

$$V_{rel,i,k} = \sqrt{u_{i,k}^2 + (\Omega_k r_{i,k} - v_{\theta,i,k})^2}. \quad (2)$$

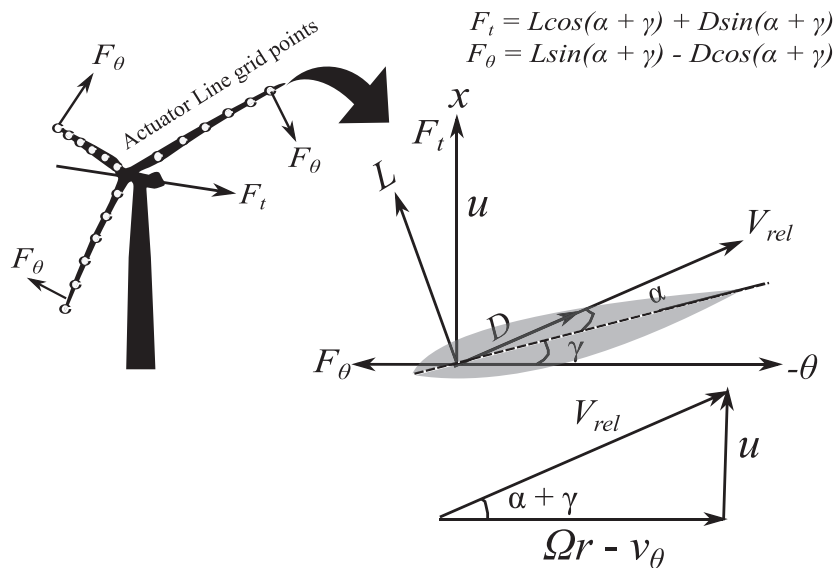


FIGURE 2 Actuator line forces obtained at different grid points (not to scale) of the turbine blades. V_{rel} obtained from the velocity triangle. F_t and F_θ are the axial thrust and rotational forces on the turbine blades due to aerodynamic lift (L) and drag (D) forces. θ : azimuthal direction, in the plane of the rotor motion. Ω : angular velocity of the rotor, r : radial distance in the blade from the center of the rotor. v_θ : azimuthal velocity of the rotor. Subscripts i, k for the local variables are omitted for clarity

Here, Ω_k is the rotor rotational speed of the turbine k , $u_{i,k}$ and $v_{\theta,i,k}$ are the local velocity components in the axial direction (perpendicular to the plane of rotation) and in circumferential direction (in the plane of rotation) obtained from large eddy simulations, and $r_{i,k}$ is the radial coordinate of each blade element. The local angle of attack $\alpha_{i,k}$ is computed as $\alpha_{i,k} = \phi_{i,k} - \gamma_{i,k}$, where $\phi_{i,k}$ is the angle between the radial velocity and the rotor plane at each blade element,

$$\phi_{i,k} = \tan^{-1} \left(\frac{u_{i,k}}{\Omega_k r_{i,k} - v_{\theta,i,k}} \right). \quad (3)$$

The total reaction force from all the actuator line elements of all the turbines experienced by the fluid is distributed smoothly across the mesh points and is given as a forcing function in the Navier-Stokes equations:

$$\tilde{\mathbf{F}}_{AL}(x, y, z, t) = - \sum_{k=1}^{N_t} \sum_{i=1}^{N_b \times N_a} (L_{i,k} \vec{e}_{L,i,k} + D_{i,k} \vec{e}_{D,i,k}) \eta_e(|\vec{r} - \vec{r}_{i,k}|), \quad (4)$$

$\vec{r} = (x, y, z)$, where $\eta_e(d)$ is a Gaussian function in the form of $\eta_e(d) = 1/e^3 \pi^{3/2} \exp[-(d/\epsilon)^2]$. $\vec{e}_{L,i,k}$, $\vec{e}_{D,i,k}$ are the local unit vectors for the lift and drag coefficients at the i th blade panel of the k th turbine. The summation in the forces is over all N_t turbines in the farm and all $N_b \times N_a$ actuator line elements per turbine, where N_b is the number of blades and N_a is the number of actuator line elements per turbine blade. The value $\epsilon = 2w_d$ is used in the current study as suggested in Troldborg²⁴ and Churchfield et al²⁴ for optimum results.

The azimuthal forces on wind turbine blade elements can be calculated as (See Figure 2 for reference)

$$F_{\theta,i,k} = L_{i,k} \sin \phi_{i,k} - D_{i,k} \sin \phi_{i,k}, \quad \phi_{i,k} = \alpha_{i,k} + \gamma_{i,k}, \quad (5)$$

which can be utilized for the computation of the aerodynamic torque for each turbine as $T_k = \sum_{i=1}^{N_b \times N_a} r_{i,k} F_{\theta,i,k} \Delta r_{i,k}$ and the power

$$P_k = T_k \times \Omega_k. \quad (6)$$

All turbines (small, intermediate, and large) are set to rotate clockwise if viewed from upstream with the prescribed constant tip speed ratio $\lambda = 5.5$, such that the rotational speed of each turbine Ω_k can be calculated as $\Omega_k = 2\lambda U_{hub,k}/D_k$, where $U_{hub,k}$ is the hub height velocity and D_k is the diameter of each turbine. The choice of prescribing a constant tip speed ratio for wind turbines is in line with previous simulations and experiments^{4,8,37,38} and corresponds to a region on a power curve between the cut-in wind speed and the rated output speed (cubic region).¹⁶ The simulations were run for 30 eddy turn over times, $30 \times (H/u_*)$, where u_* is the friction velocity above the wind turbine canopy involving large turbines (case L), to ensure statistical stationarity of the results. Unless otherwise mentioned, all the statistical and spectral results involve normalization with mean free-stream velocity scale, U_∞ . Power was normalized with U_∞^3 .

3 | RESULTS: POWER AND PERFORMANCE

In this section, the performance of the multiscale wind farm is assessed in terms of power and its variability for wind turbines operating at different scales (large and small/intermediate turbines) and compared against corresponding single-scale, homogeneous, cases in similar configurations. The total power extracted by wind turbines in a wind farm can be defined as

$$P = \sum_{k=1}^{N_t} \frac{\overline{P_k(t)}}{U_\infty^3}, \quad (7)$$

where N_t is the total number of the turbines in wind farm ($N_t = 9$ in all single-scale cases, $N_t = 18$ in all multiscale cases). In Equation 8, the power $P_k(t)$ is the power of the k th turbine in the computational domain calculated from Equation 6 and, as discussed earlier, further normalized with U_∞^3 for a consistent comparison between the cases. $\overline{P_k(t)}$ refers to a temporally averaged value of $P_k(t)$. It is also useful to define the mean power density, which can be calculated by dividing the total power in wind farm by the wind farm area $A_{farm} = N_t^{\xi} s_x s_y D_L^2$ as $\rho_m = P/A_{farm}$, where P is the total power extracted by the wind farm defined by Equation 7.

To compare the turbines operating at each particular scale, it is also useful to define the mean power and variability of turbines at each scale. Mean turbine power at each scale of operation can be defined as

$$P_{m,\xi} = \frac{1}{N_t^\xi} \sum_{k \in \xi: k=1}^{N_t^\xi} \frac{\overline{P_k(t)}}{U_\infty^3}, \quad (8)$$

where ξ is the set of the turbines of the same scale and N_t^ξ is the number of the turbines of the same scale ($\xi = L, S, I$) in single-scale or multiscale arrangements ($N_t^\xi = 9$ for all the simulated cases). Note that at some instances in the manuscript, we will be referring to a time-dependent turbine-averaged mean power for each turbine scale defined as

$$P_{m,\xi}(t) = \frac{1}{N_t^\xi} \sum_{k \in \xi: k=1}^{N_t^\xi} \frac{P_k(t)}{U_\infty^3}, \quad (9)$$

TABLE 5 Comparison of MKE flux difference $\Delta\Phi_p$ and mean power density ρ_m for all the single-scale and multiscale wind farm cases^a

Case	ρ_m	$\Delta\Phi_p$	%Deviation
L	2.61×10^{-3}	2.65×10^{-3}	+1.5%
S	5.43×10^{-4}	5.70×10^{-4}	+5.0%
I	6.81×10^{-4}	6.97×10^{-4}	+2.3%
LS^M	3.14×10^{-3}	2.93×10^{-3}	-6.7%
LI^M	3.22×10^{-3}	2.95×10^{-3}	-8.3%

^aBoth $\Delta\Phi_p$ and ρ_m are normalized with U_∞^3 .

where instantaneous, and not a temporally averaged power, is further averaged among all the turbines of the same scale in a wind farm.

The mean power variability due to turbulence for wind turbines operated at the same scale can be further measured using the definition of coefficient of variation (standard deviation of a temporal power of a turbine normalized by a temporally averaged power of a turbine) and averaged over the turbines as in Equation 10,

$$V_{m,\xi} = \frac{1}{N_t^\xi} \sum_{k \in \xi: k=1}^{N_t^\xi} \sqrt{\frac{\overline{(P_k(t)^2 - \bar{P}_k(t)^2)}}{\bar{P}_k(t)}}. \quad (10)$$

In the comparison of power and variability in the tables below, a case format X/Y has been used, which manifests the fact that the percentage gain/loss in case X has been compared against case Y, as $(X - Y)/Y \times 100\%$. For brevity and easy reference, throughout the subsequent sections, cases LS^M , LI^M are also denoted as “vertically staggered” or “multiscale,” and cases L, S, I as “homogeneous” arrangements. Note that the word “homogeneous” refers here to the fact that the turbines in the wind farm are all of the same kind, ie, homogeneous, and not to the state of the turbulence, which is clearly inhomogeneous in all three directions due to the presence of wind turbines.

3.1 | Overall wind farm performance

We first calculate the mean turbine power density ρ_m for all five considered cases and compare it with the mean kinetic energy (MKE) flux difference $\Delta\Phi_p$ in Table 5 (both normalized with U_∞^3). The MKE flux difference in single-scale layouts is defined as $\Delta\Phi_p = \phi(z_h + D/2) - \phi(z_h - D/2)$, where z_h , D are the hub height and the rotor diameter of the turbines and the MKE flux $\phi = -\overline{u'w'}\bar{U}$, where $-\overline{u'w'}$ is the kinematic shear stress, \bar{U} is the streamwise velocity (both terms are horizontally and temporally averaged) at the top and bottom tip of the turbines. The definition needs to be slightly modified for multiscale layouts as $\Delta\Phi_p = \phi(z_h + D_L/2) - \phi(z'_h - D_S/2)$, where z'_h , z_h are the hub heights of the small/intermediate and large turbines, respectively, since the bottom tip of the small/intermediate turbines is always the lowest, and the top tip of the large turbines the highest, in the vertically staggered cases considered here.

The equivalence of the two terms (ρ_m and $\Delta\Phi_p$) was first demonstrated for a single-scale wind farm by vertical integration of the temporally and horizontally averaged kinetic energy equation between the turbine rotor bottom and top tip location.³⁹ However, it can be extended quite straightforwardly to multiscale wind farm cases by changing the bottom and top limits of integration to $z'_h - D_S/2$, $z_h + D_L/2$, respectively. As can be seen from Table 5, an absolute value of the deviation of less than 8% is observed for all the cases, consistent with the findings of Calaf et al.³⁹

We now document the overall power gain in multiscale wind farms (cases LS^M , LI^M) compared with a baseline large-scale wind farm configuration (case L) in Table 6A. As expected, a significant power gain of around 20% is achieved in both cases, due to the fact that an additional power capacity in the form of the small/intermediate turbines was added. To assess the individual performance and efficiency of the turbines at each scale, it is instructional to compare the power change in a multiscale wind farm against the direct sum of the powers in corresponding isolated homogeneous wind farms featuring large- and small/intermediate-scale turbines only, which is shown in Table 6B. Note that statistical uncertainty in the calculated wind farm power was estimated to lie within 0.25% bound for all the cases using the analysis of the coefficient of variation between the available sampling groups,¹⁸ while the maximum uncertainty in the power gain or loss during the relative comparison between the cases is roughly twice this number, ie, about $\lesssim 0.5\%$ for all the cases. The same uncertainty bounds are applied to the power variability.

In the following analysis, we look at the performance of large and small wind turbines separately in a multiscale wind farm, in order to elucidate the effects of interaction between the turbines of different scales, and how these interactions influence the turbine operation compared with homogeneous environments.

3.2 | Large turbines

To further assess the turbine performance, it is useful to look at the mean power of wind turbines at each scale. Temporal variation in the mean power generated by the large and small/intermediate turbines in vertically staggered and homogeneous layouts containing large turbines

TABLE 6 Change in total power in multiscale wind farms (A) with addition of small/intermediate turbines and (B) as compared with the direct sum in isolated homogeneous wind farms

Case	$\Delta P_{X/Y}$
A	
LS^M/L	+20.45%
LI^M/L	+23.25%
B	
$LS^M/(L + S)$	-0.28%
$LI^M/(L + I)$	-2.45%

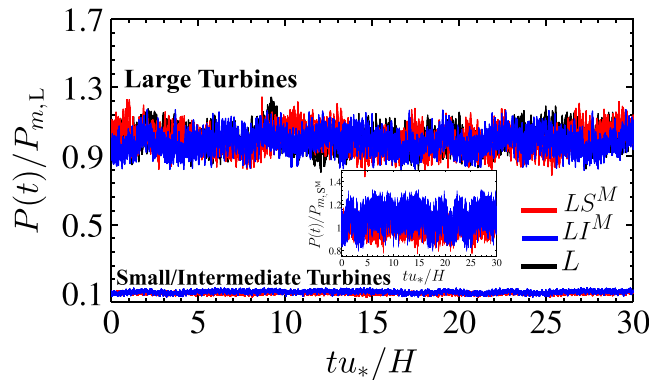


FIGURE 3 Temporal variation of the mean power (see Equation 9) in cases containing large turbines: power of large turbines in cases L , LS^M , LI^M , as well as small/intermediate turbines in cases LS^M , LI^M , normalized with the mean power $P_{m,L}$ of baseline case L . Inset: power of the small/intermediate turbines in cases LS^M , LI^M normalized with the mean power of the small turbines $P_{m,SM}$ in case LS^M [Colour figure can be viewed at wileyonlinelibrary.com]

TABLE 7 Change in mean power and variability in large and small/intermediate turbines in multiscale wind farms compared with their homogeneous counterparts of equivalent hub heights. (A) Large turbines: $L^M(LS^M)$ – large turbines in LS^M layout, $L^M(LI^M)$ – large turbines in LI^M layout. (B) Small/intermediate turbines

Case	$\Delta P_{m,X/Y}$	$\Delta V_{m,X/Y}$
A		
$L^M(LS^M)/L$	-0.99%	-1.78%
$L^M(LI^M)/L$	-0.54%	+10.7%
B		
S^M/S	+3.87%	-33.6%
I^M/I	-8.8%	+32.9%

is shown in Figure 3. It can be seen that the mean power P_m of the large turbines in multiscale layouts (LS^M , LI^M) does not change significantly (approximately 1%) compared with the baseline case L (see Table 7A). However, while the change of power variability in large turbines in case LS^M against case L is not noticeable, variability of power in large turbines in case LI^M shows approximately 10% increase compared with baseline case L possibly due to its interaction with the intermediate turbines. These findings are inline with approximately 5% power variability increment in large wind turbines in a vertically staggered farm (containing HAWTs and VAWTs) compared with HAWT-only farm of Xie et al.¹⁵

3.3 | Small/intermediate turbines

Figure 4 and Table 7B document the comparison of power in the small and intermediate turbines in a vertically staggered layout against the homogeneous arrangements with the same hub heights. It is interesting to note that small turbines in a vertically staggered configuration (LS^M) are power efficient and manifest a gain of approximately 4% in mean power compared with a homogeneous arrangement (S), with a substantial decrease in variability by more than 30%. For intermediate turbines in vertically staggered farms (LI^M), the power comparison results show a

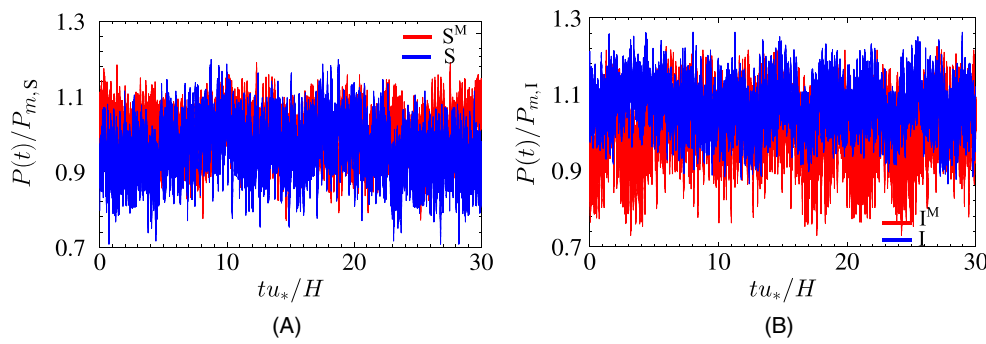


FIGURE 4 A comparison of the temporal variation of the mean power (see Equation 9) of small/intermediate wind turbines in a vertically staggered (LS^M, LI^M) and homogeneous arrangements (S, I). A, Small turbines S, S^M with hub height $z'_h = 0.3D_L$; B, intermediate turbines I, I^M with hub height $z'_h = 0.6D_L$. $P_{m,\xi}$ ($\xi = S, I$) denote the mean power of small/intermediate turbines in a homogeneous, single-scale orientation [Colour figure can be viewed at wileyonlinelibrary.com]

TABLE 8 Relative change in mean power from small to intermediate turbines when hub height increased from $0.3D_L$ to $0.6D_L$, and rotor radius fixed at $D_S = 0.3D_L$

Case	Mean power gain
Homogeneous (I / S)	+25.15%
Vertically staggered (I^M / S^M)	+10.29%

completely opposite behaviour; ie, they are *inefficient* manifesting a significant approximately 9% drop in power and an increase in variability by greater than approximately 30% against homogeneous wind farms with the same hub heights (I). This is further corroborated in Table 8, where we observe that the mean power growth is significantly suppressed when the hub heights of the small wind turbines are doubled in the vertically staggered arrangement.

From the above discussion, it is apparent that while the addition of the small turbines does not illustrate a prominent negative influence on the performance of the large turbines, the presence of the large turbines significantly affects the performance of the small/intermediate ones. It is evident that for the case LS^M , the small turbines (that lie completely outside the wakes of the large turbines) are able to harvest more energy per turbine than they would do otherwise in isolated homogeneous wind farms with the same small-turbine layout (S), perhaps by efficient utilization of the organized, coherent structures generated by large turbines, which also amounts to reduced variability. A further evidence that the organized structures might be responsible for the power increase was also observed in the energy spectra plots discussed in Section 3. For intermediate turbines at hub heights of $0.6D_L$ (which are partially in the wakes of the large turbines), on the other hand, the interference is destructive compared with the intermediate-turbine only arrangements I , with less power and higher variability in the intermediate turbines in vertically staggered wind farms, possibly coming from stronger direct interactions between the large and intermediate turbines due to their relative proximity, wake impingements, and a modulation of coherent structures.

3.4 | Joint probability density function

The analysis can be further extended by the joint probability density function (jpdf) of the power of the large and small/intermediate turbines in the multiscale layouts. For two random variables X and Y , a joint probability density function jpdf is related to a joint cumulative distribution function jcdf (a probability that X is no greater than \bar{x} and Y is no greater than \bar{y}) as $jcdf(\bar{x}, \bar{y}) = \int_{-\infty}^{\bar{x}} \int_{-\infty}^{\bar{y}} jpdf(x, y) dx dy$. In a discrete computation, jpdf can be extracted from the envelope of a 3D histogram plot that computes the relative frequency of occurrence of the events within the specified bin values. If the random variables within the bin $[(x_1, x_2), (y_1, y_2)]$ are considered, the relative frequency of occurrence within this bin can be defined as N_{bin}/N_{tot} , where N_{bin} is the number of events falling within the bin and N_{tot} is the total number of the events. The relative frequency of occurrence (probability that the variables are within the bin) is related to jpdf as $N_{bin}/N_{tot} = jpdf \times A_{bin}$, where A_{bin} is the bin area, from where jpdf can be estimated by dividing the relative frequency by the bin area (frequency density). To obtain a smooth approximation from a discrete distribution data, a smoothing procedure in the form of a two-dimensional kernel density estimation from MATLAB toolbox was used to calculate the joint pdf. The corresponding jpdf for the power of the large and small/intermediate turbines in the multiscale layouts LS^M, LI^M is plotted in Figure 5, where the normalized power $\bar{P}_{LM}, \bar{P}_{IM}, \bar{P}_{SM}$ (normalized by the mean power of the large turbines in each multiscale layout) is considered as random variables in the 3D histogram plot and in jpdf. The convergence criterion $\int_{-\infty}^{\infty} \int_{-\infty}^{\infty} jpdf(\bar{P}_{LM}, \bar{P}_{\xi^M}) d\bar{P}_{LM} d\bar{P}_{\xi^M} = 1$, $\xi = S, I$, is satisfied by the algorithm with the tolerance of 10^{-4} . Thus defined, jpdf essentially represents the rate of change of probability of a joint event with $\bar{P}_{LM}, \bar{P}_{\xi^M}$, when the values of random variables change from \bar{P}_{LM} to $\bar{P}_{LM} + \Delta\bar{P}_{LM}$, and from \bar{P}_{ξ^M} to $\bar{P}_{\xi^M} + \Delta\bar{P}_{\xi^M}$, $\xi = S, I$. The jpdf in Figure 5 indicates that the higher power in the large turbines is well correlated with the higher power of the small turbines in the same multiscale layout. From the high jpdf regions of the contour (a region of higher probability density, $jpdf(\bar{P}_{LM}, \bar{P}_{\xi^M}) > 150$), it is apparent that in case LS^M , for a

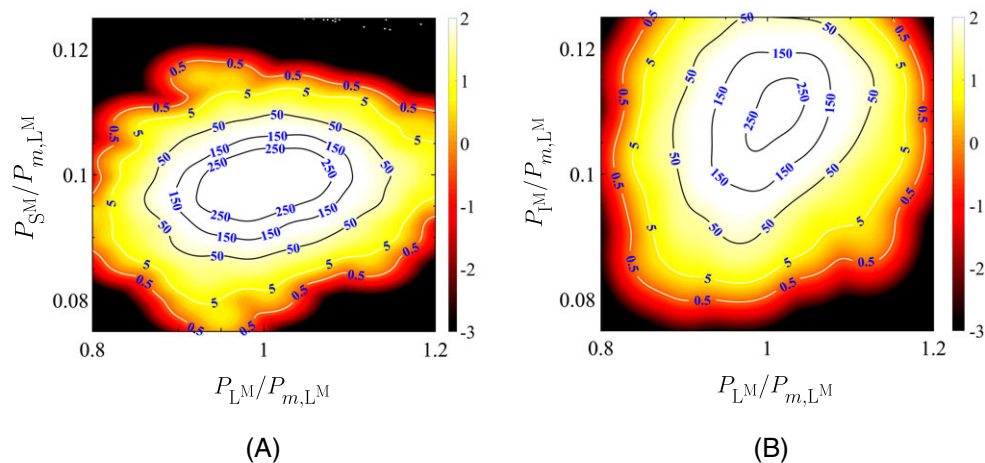


FIGURE 5 Two-dimensional joint probability density function $\text{jpdf}(\bar{P}_{L^M}, \bar{P}_{\xi^M})$ of wind turbine power for the turbines L^M, ξ^M . $\xi = S, I$: A, case LS^M ; B, case LI^M . All power variables are normalized with P_{m,L^M} , which is the mean power of the large turbines in LS^M and LI^M for A and B, respectively. Color contours— $\log_{10} (\text{jpdf}(\bar{P}_{L^M}, \bar{P}_{\xi^M}))$. Labeled contour lines— $\text{jpdf}(\bar{P}_{L^M}, \bar{P}_{\xi^M})$ overlayed on the top of color contours. Colormap axis— $[10^{-3} 10^2]$. The jpdf satisfies $\int_{-\infty}^{\infty} \int_{-\infty}^{\infty} \text{jpdf}(\bar{P}_{L^M}, \bar{P}_{\xi^M}) d\bar{P}_{L^M} d\bar{P}_{\xi^M} = 1$ [Colour figure can be viewed at wileyonlinelibrary.com]

wide variation of power in large turbines, we have significantly less variation of power in the small turbines, a feature not seen in case LI^M . This illustration with joint pdf indicates the fact, that the power of small wind turbines at hub height $z'_h = 0.3D_L$ comes from more well-organized structures than that of the intermediate turbines at hub height $z'_h = 0.6D_L$.

4 | RESULTS: FLOW ANALYSIS

Further insights regarding the physical mechanisms responsible for the change in power and variability in the multiscale wind farm arrangements will be discussed through the mean and the second-order turbulent statistics, as well as the energy spectra, in the subsequent section.

4.1 | Mean and turbulent statistics

In a conventional, homogeneous, periodic wind farm, it is known that the horizontally and temporally averaged mean streamwise velocity profile $\langle \bar{u} \rangle$ (–, temporal, and $\langle \rangle$, xy averaging) manifests a double log layer in the vertical direction, induced by the bottom wall roughness $z_{0,lo} = z_0$ (lower log layer) as well as the wind turbine roughness $z_{0,hi} > z_{0,lo}$ (top log layer).³⁹ Lettau roughness⁴⁰ is a measure of the geometric roughness $z_{0,hi}$ imposed by the organized array of wind turbines in addition to the roughness due to the topography of the land. The Lettau roughness⁴⁰ is given as $z_{0,\text{Let}} = 0.5hS/A$, where h is the effective height of the obstacle posing as a roughness, S is the silhouette area seen by the wind in the cross-wind-lateral direction (shadow area of the obstacle projected in the plane), and A is the specific lot area measured in the horizontal plane or plane described by the average earth/air surface and is representative of how densely packed the roughness obstacles are. The numerical factor 0.5 corresponds to the average drag coefficient of the characteristic individual obstacle of silhouette area. For multiscale wind farms, this formula can be potentially modified as $z_{0,\text{Let}} = 0.5(n_t^L z_h S_L + n_t^S z'_h S_S)/A$, where n_t^L, n_t^S is the number of large and small/intermediate wind turbines at a lot of area A , z_h , and z'_h are hub heights of the large and small/intermediate wind turbines, respectively, as defined previously, and $S_L = \pi D_L^2/4$, $S_S = \pi D_S^2/4$ are the rotor areas of the large and small/intermediate turbines. In our multiscale wind farm cases, $n_t^L = n_t^S = 1$ at a lot of area $A = s_x s_y D_L^2$ (either n_t^L or n_t^S is zero in single-scale wind farms), which results in Lettau roughness presented in Table 9 for all the cases.

Table 9 indicates that the roughness of the small/intermediate turbines-only configurations is more than an order of magnitude smaller than their large-only counterpart. Consequently, the contribution of the small turbines into the overall roughness in multiscale wind farms is less significant, and the roughness in cases LS^M, LI^M is mostly defined by the roughness of large turbines, as seen from Table 9. The roughness values influence the mean streamwise velocity profile in Figure 6 that shows distinct double log-layer trends in cases L, LS^M, LI^M with a significant degree of overlap (with the major discrepancies occurring in the region of mixing, $z_h - D_L/2 < z < z_h + D_L/2$), and essentially a single logarithmic trend in Cases S, I .

TABLE 9 Lettau roughness of the large and small/intermediate single-scale wind farms (L, S, I), as well as the multiscale configurations LS^M, LI^M normalized by aerodynamic roughness

Case	L	S	I	LS^M	LI^M
z_{Lett}/z_0	61.71	1.72	3.34	63.43	65.05

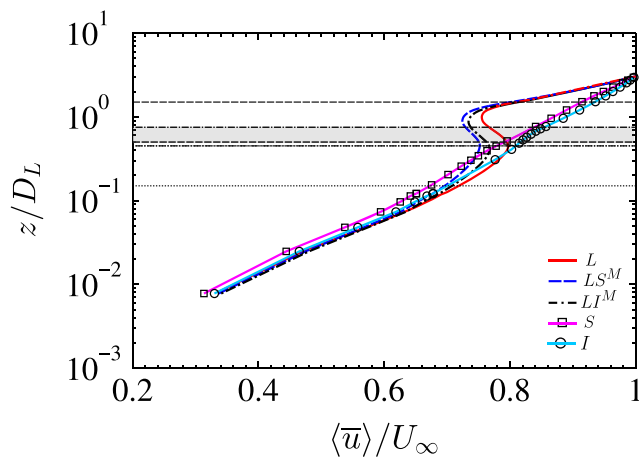


FIGURE 6 Temporally and horizontally averaged mean streamwise velocity $\langle \bar{u} \rangle / U_\infty$. Horizontal lines at the top and bottom tip of turbine rotors: dashed, large turbines; chain dotted, intermediate turbines; dotted, small turbines; gray patch, overlap area between large and intermediate turbine in LI^M [Colour figure can be viewed at wileyonlinelibrary.com]

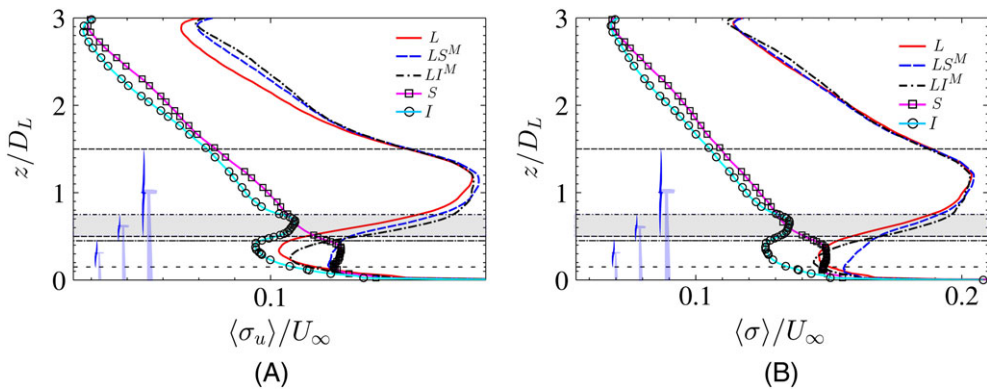


FIGURE 7 Temporally and horizontally averaged A, streamwise turbulence intensity σ_u / U_∞ , where $\sigma_u = \sqrt{\bar{u}'^2}$, and B, total turbulence intensity σ / U_∞ , where $\sigma = \sqrt{\bar{u}'^2 + \bar{v}'^2 + \bar{w}'^2}$. Normalization by mean free stream velocity scale U_∞ . Rotor swept area shown as horizontal lines at the top and bottom tip of the turbine rotor with a wind turbine schematic: dashed, large turbines; chain dotted, intermediate turbines; dotted, small turbines; gray patch, overlap area between the large and intermediate turbine in LI^M [Colour figure can be viewed at wileyonlinelibrary.com]

Figure 7 depicts the horizontally averaged turbulence intensity for the homogeneous and multiscale wind farms. Expectedly, the homogeneous wind farms with small/intermediate turbines (S, I) show much smaller turbulence intensity throughout the domain than the homogeneous farms with large turbines (L) or the multiscale arrangements (LS^M, LI^M). In general, turbulence intensity profiles from the u' fluctuations alone and from the sum of the components ($\bar{u}'^2 + \bar{v}'^2 + \bar{w}'^2$) are fairly similar in magnitude and shape, allowing for an argument that most of the turbulent activity around the turbine rotors comes from the streamwise fluctuations. The exception is the region near the hub heights of the small turbines ($z_h' = 0.3D_L$) in the multiscale arrangement, suggesting that, perhaps, other components play an increasingly important role in the structure of turbulence and the power production of the small turbines in this case.

4.2 | Wake recovery

Insights from the power generated by the wind turbines can be gained by studying the wake recovery of the mean velocity profile around the large and small turbines. From Figure 8A, we observe that for the baseline homogeneous case of large-only turbines L as well as the vertically staggered cases LS^M, LI^M , the wake recovery of the large turbines in the location $z_h - D_L/2 < z < z_h + D_L/2$ ($z_h = D_L$) remains similar, as is expected from the fact that the power in the large turbines was found to be similar across the cases. The recovery of the velocity deficit regions is also associated with the decay of the turbulence intensity and the kinematic shear stress ($\sigma_u, -\bar{u}'\bar{w}'$) in the turbine rotor swept region. It was observed that in general, the streamwise turbulence intensity and kinematic shear stress ($\sigma_u, -\bar{u}'\bar{w}'$) are slightly increased in the cases LS^M, LI^M compared with L, supposedly due to the addition of the smaller turbines. However, for the small and intermediate turbines, (Figure 9A-D), it is apparent that the wakes ($z_h' - D_S/2 < z < z_h' + D_S/2, z_h' = 0.3D_L$, small; $z_h' = 0.6D_L$, intermediate) in vertically staggered orientation are affected by the wakes of the large turbines. Thus, while the wakes of the small/intermediate turbines recover smoothly in the homogeneous arrangement (S, I), bulges corresponding to high velocity regions of the large turbines appear at around $z \approx 0.3D_L$ for LS^M, LI^M , expediting the wake recovery

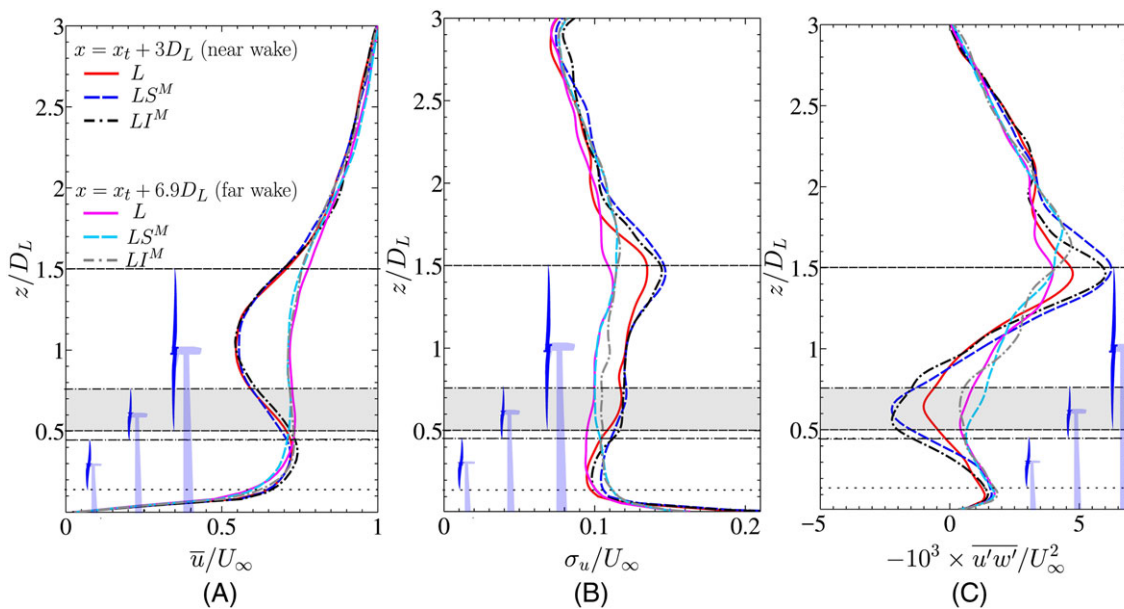


FIGURE 8 Spanwise averaged mean and turbulent statistics focused on wake recovery of the large turbines. A, Mean streamwise velocity \bar{u} ; B, streamwise turbulent fluctuations $\sigma_u = \sqrt{\bar{u}'^2}$; C, kinematic shear $-\bar{u}'w'$. Variables normalized by free stream velocity U_∞ . x_t : Large turbine location in row L2 (see Figure 1). Rotor swept area shown as horizontal lines at the top and bottom tip of the turbine rotor with a wind turbine schematic: dashed, large turbines; chain dotted, intermediate turbines; dotted, small turbines; gray patch, overlap area between the large and intermediate turbine in LI^M [Colour figure can be viewed at wileyonlinelibrary.com]

for case LS^M while no such benefit occurs for case LI^M . These observations are in concordance with the power of the turbines documented in section 3.3. Furthermore, near the rotor-swept regions of small turbines, cases S, I show a marked difference in the mean and turbulent statistics with the cases LS^M, LI^M since the small turbines in the latter are influenced by the dynamics of the large wind turbines. Specifically, the influence of the large turbines on the small or intermediate ones is illustrated by the disparate distances (scales) of the wake recovery, the decay of turbulent statistics in the rotor swept region, and the differences in shear stress behavior. The results obtained from the above flow analysis and the turbine power data are seen to be inline with a recent study by Vasel-Be-Hagh and Archer¹⁴ who have also found that a larger difference in hub heights is more effective than a smaller difference in vertically staggered arrangements. The authors identified two competing effects for the lower turbines: The presence of increased shear reduces power, but a larger rotor area that is not exposed to the upstream wakes can increase power. It was concluded that the latter effect dominates when the spacing is tight between the turbines.¹⁴

Figure 10 showing the temporally filtered velocity magnitude contours further corroborates the fact that the flow features around the large wind turbines are mainly unaffected in the multiscale arrangements, while features around the small wind turbines are influenced by the presence of the large ones. Visual analysis of the structures shed by the large turbines corroborates the fact that they are produced in the shear layer at the bottom rotor tip and are entrained below the large turbine rotors, consistent with the previous spectral analysis.^{17,18} For the small turbines at lower hub heights, these organized structures impinge directly on the turbine rotors and are harvested efficiently by the small turbines, increasing their power and reducing variability. For the intermediate turbines at higher hub heights, the structures pass below the rotors, leaving the intermediate turbines face an incoherent wake of large turbines, decreasing the power and increasing variability in intermediate turbines.

4.3 | Premultiplied spectra

The 1D streamwise and wall normal energy spectra of the turbulent flow field of the single-scale wind farms is illustrated in Figure 11 for the cases L, LS^M, LI^M . Note that the flow is not spatially homogeneous due to the presence of wind turbines. Hence, the energy spectra is defined as the inverse Fourier transform of the horizontally averaged 2-point correlation of the velocity fluctuations thus owing to the horizontal periodicity of the domain. For more details regarding the definition of spatial energy spectra in periodic wind farms, the reader is referred to Chatterjee and Peet.¹⁸ The spanwise-averaged 1D premultiplied streamwise and wall-normal energy spectra ($k_x E_{uu}, k_x E_{ww}$) in Figure 11B,C indicate that except for a slight discrepancy at length scales $\lambda_x > D_L$, the u, w energy spectra at and above the hub height $z = D_L$ of the large turbines remain the same for the cases L, LS^M, LI^M . Interestingly, it is also observed that the wall-normal kinetic energy at length scales $\lambda_x \leq D_L$ is much larger than the streamwise counterpart at these locations, manifesting a potential signature for the downdrafts of energetic structures from the top of the boundary layer. This, again, is in agreement with the fact that the power production in large turbines is not influenced (augmented or destructed) by the addition of the smaller-scale turbines in the bottom layer in this multiscale HAWT wind farm.

It is instructive to note that the peaks in the 1D u, w spectra (Figure 11B) at the hub height of the large turbines are a manifestation of the interception of eddies by the rotating turbine blades. Furthermore, the “wiggles” that are observed in the spectra at the hub height are actually

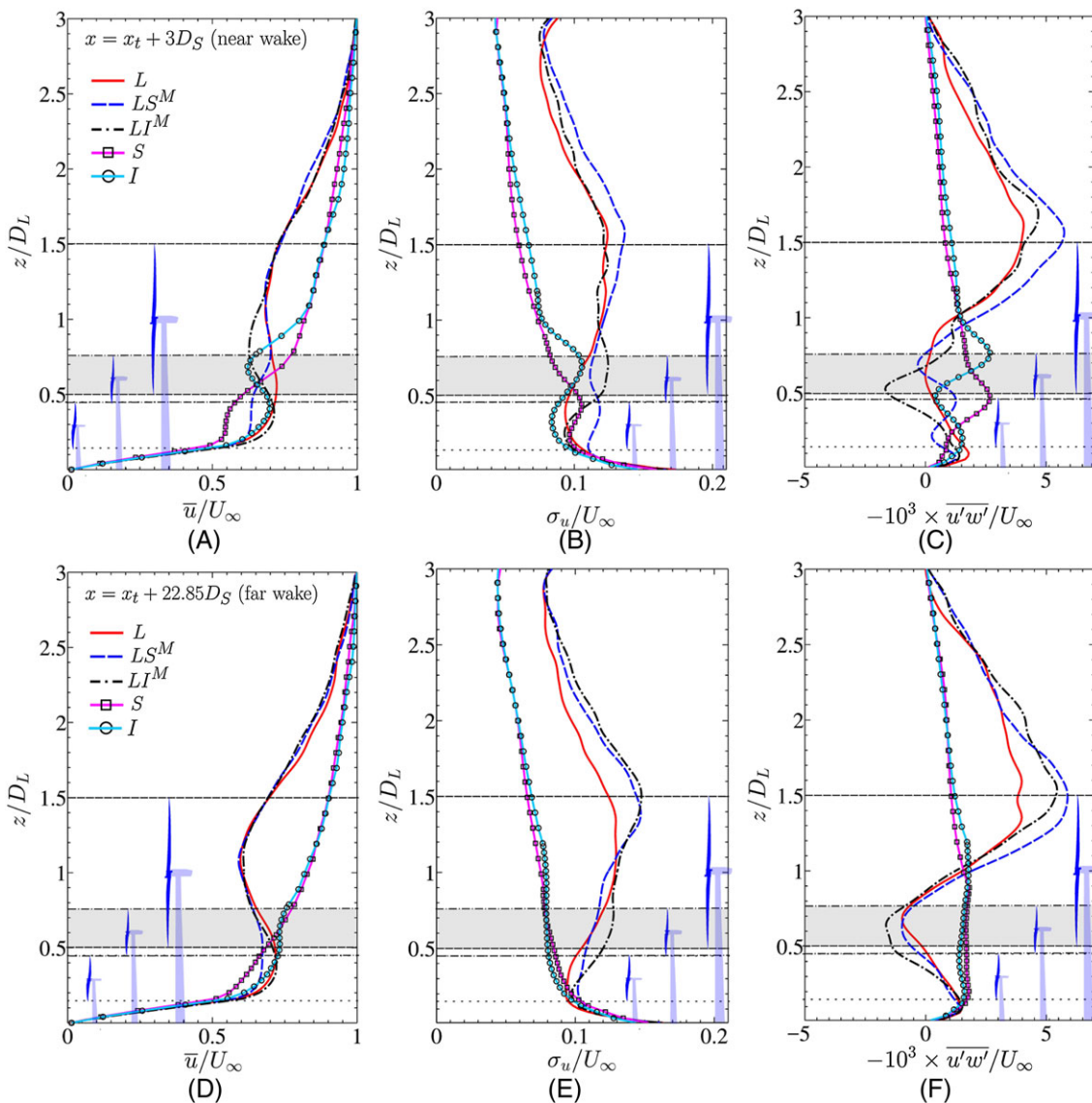


FIGURE 9 Spanwise averaged mean and turbulent statistics focused on wake recovery of the small/intermediate turbines. A and D, mean streamwise velocity \bar{u} ; B and E, streamwise turbulent fluctuations $\sigma_u = \sqrt{\overline{u'^2}}$; C and F, kinematic shear $-\overline{u'w'}$. Variables normalized by free stream velocity U_∞ . x_t : Small turbine location in row 2 (see Figure 1). Rotor swept area shown as horizontal lines at the top and bottom tip of the turbine rotor with a wind turbine schematic: dashed, large turbines; chain dotted, intermediate turbines; dotted, small turbines; gray patch, overlap area between the large and intermediate turbine in L^M [Colour figure can be viewed at wileyonlinelibrary.com]

the higher wave number harmonics of the fundamental wave number corresponding to the periodicity imposed by the large wind turbine rows. To address this, we first identify the peak at the largest wavelength at Figure 11B corresponding to $\lambda_x = 7D_L$. This is the peak corresponding to the streamwise separation between the large turbine rows, which in a periodic WTABL framework imposes its own inherent periodicity at hub height, with the turbine raw separation. All the subsequent peaks to the left of the main peak correspond to the wave numbers of $2k_0, 3k_0, 4k_0$, and so on, where $k_0 = 2\pi/(7D_L)$ is the fundamental wavenumber corresponding to the largest peak. The reason for these superharmonics can be understood from the terms in the Fourier series of a periodic signal with the fundamental frequency k_0 , which is however not a pure sine or cosine signal. Such a signal, when expanded in Fourier series would have components of the multiples of frequency k_0 , such as $k_0, 2k_0, 3k_0, 4k_0$. This observation is further corroborated by the fact that the spectra in the inner layer and the outer layer do not contain similar peaks or wiggles, since they lie outside of the turbine rotor area where the streamwise periodicity due to the rotor placement no longer plays a role.

Close to the “wall” at $z = 0.075D_L$ (Figure 11A), we do not observe any streamwise length scales at which the wall-normal spectra dominates its streamwise counterpart. This indicates the presence of quasi-inviscid 2D “inactive” eddy structures, as observed in our previous work.²³ This phenomenon corroborates towards the evidence of vertical turbulent motions from the outer layer towards the “wall” in cases L , LS^M , and L^M . Whether these vertical motions can be utilized for power, depends on the organization of structures at the top of the rotor of the smaller turbines and discussed further in the 2D spectra. The experimental studies by Hamilton et al⁴¹ and Chamorro et al¹⁹ as well as our recent numerical studies¹⁸ have revealed the contribution of length scales larger than rotor diameter to the wind turbine power. With these observations in mind,

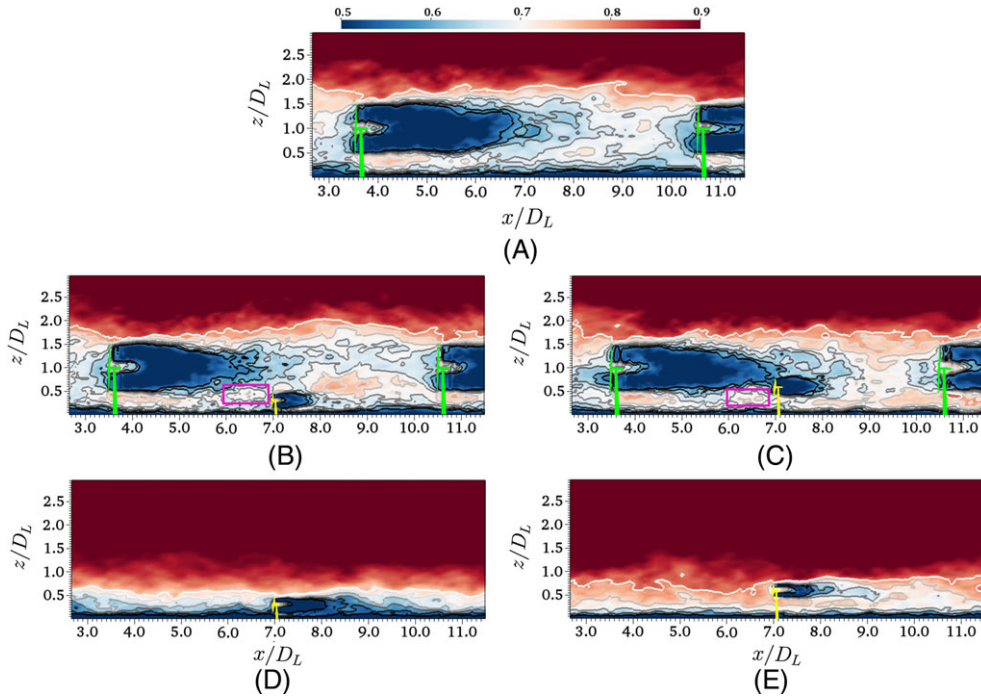


FIGURE 10 xz plane ($y = 4.5D_L$) of normalized velocity magnitude $\sqrt{u^2 + v^2 + w^2}/U_\infty$ in vertically staggered and homogeneous wind farms, temporally averaged for 10 eddy turn over times, based on the friction velocity of large turbines. A, baseline case L; B, case LS^M ; C, case LI^M ; D, case S; and E, case I. Contour lines in grayscale: 0.575 to 0.8 of U_∞ . The solid magenta colored windows in cases LS^M and LI^M point to energetic structures around small and intermediate turbines (above for small turbines and below for intermediate turbines) present in multiscale arrangements that are not seen in homogeneous cases S, I. Large, intermediate, and small turbines are schematically shown in color [Colour figure can be viewed at wileyonlinelibrary.com]

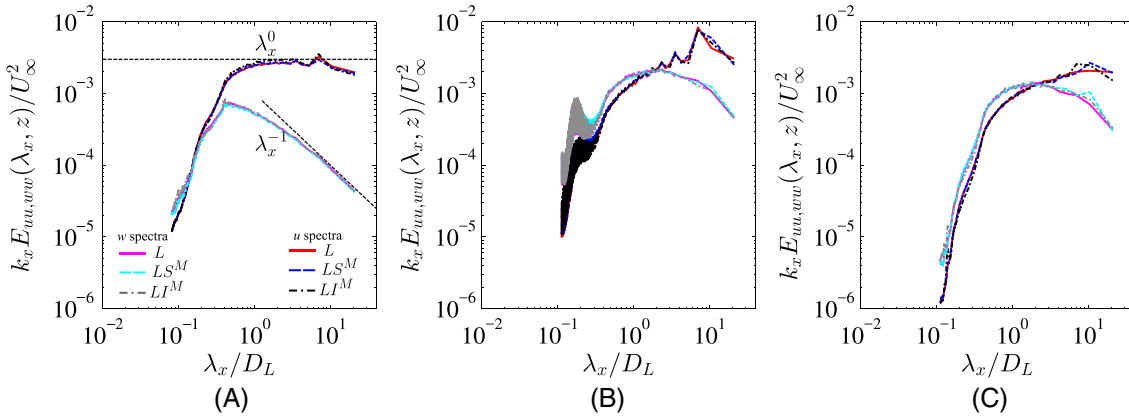


FIGURE 11 One-dimensional premultiplied streamwise and wall normal energy spectra $k_x E_{uu}$, $k_x E_{ww}$ for cases L, LS^M , LI^M . A, inner layer, $z = 0.075D_L$; B, at hub height of large turbines $z = D_L$; C, outer layer, $z = 2.25D_L$. λ_x^0 , λ_x^{-1} are corresponding near-wall k_x^{-1} and k_x^0 scaling of E_{uu} and E_{ww} spectra in the neutral ABL²³ [Colour figure can be viewed at wileyonlinelibrary.com]

we analyze the 2D premultiplied energy spectra of the multiscale as compared with single-scale homogeneous wind farm cases with an emphasis on such energetic eddies with the scales in the range $D - 10D$ in Figures 12 to 15.

We first observe that the presence of the small-scale turbines does not significantly affect the spectra and energetic eddies around the large turbines (cases L, LS^M , LI^M), consistent with our previous observations. As seen from the almost identical contours of the streamwise energy spectra of cases L, LS^M , LI^M around the rotor-region of large turbines in Figures 12 and 13, it appears that the presence of small turbines has almost no influence on the larger length scales of the u energy spectra. On the contrary, the influence of the large turbines is prominently seen in the streamwise energy spectra of the flow around the rotor-swept region of the small/intermediate turbines (see Figures 14, 15). The small/intermediate turbines in LS^M , LI^M are separately compared against the turbines in cases S, I, respectively, to analyze the effects of their interaction with large turbines. While in the multiscale wind farm LI^M , we observe energy in the top, $z'_h + D_S/2$ and the bottom $z'_h - D_S/2$ of the rotor tip to be concentrated at larger length scales, $\lambda_x > D_L$, in the wind farm LS^M , we observe a markedly different phenomenon. Even though the energy at the top rotor tip, $z'_h + D_S/2$, is concentrated at larger length scales, $\lambda_x > D_L$, the energy at the bottom rotor tip, $z'_h - D_S/2$ is

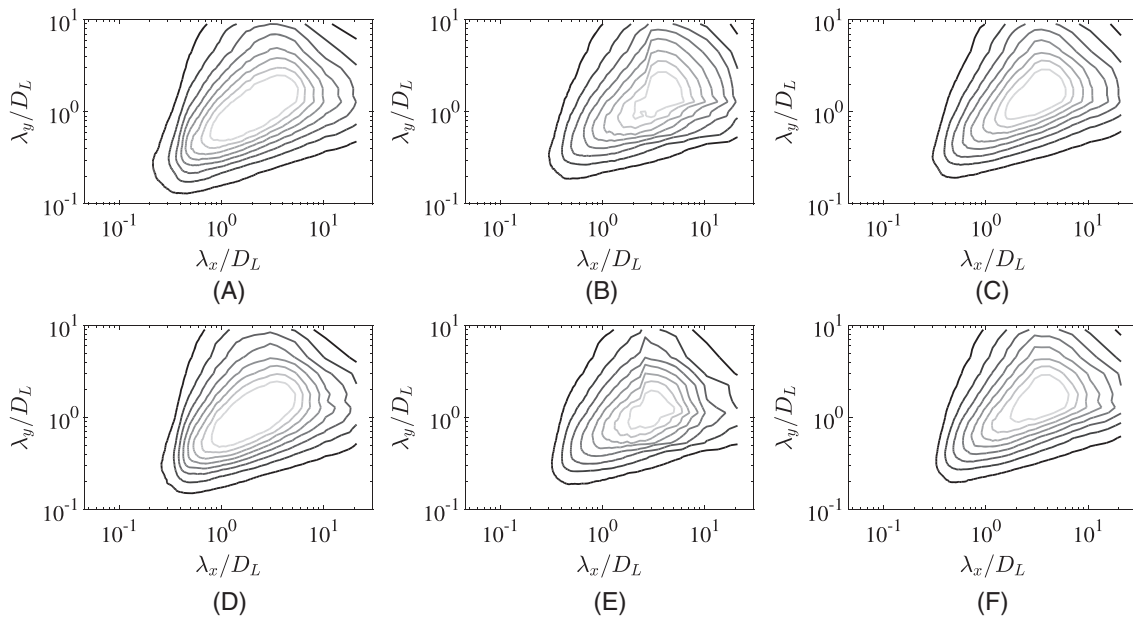


FIGURE 12 Two-dimensional premultiplied streamwise energy spectra $k_x k_y E_{uu} / U_\infty^2$ of the large turbines, top row: LS^M ; bottom row: L . A and D, $z = z_h - D_L/2$; B and E, $z = z_h$; and C and F, $z = z_h + D_L/2$. Contour levels: 10% to 80% of maximum, with the separation of 10% per each contour line, higher energy content is at lighter shades of grey

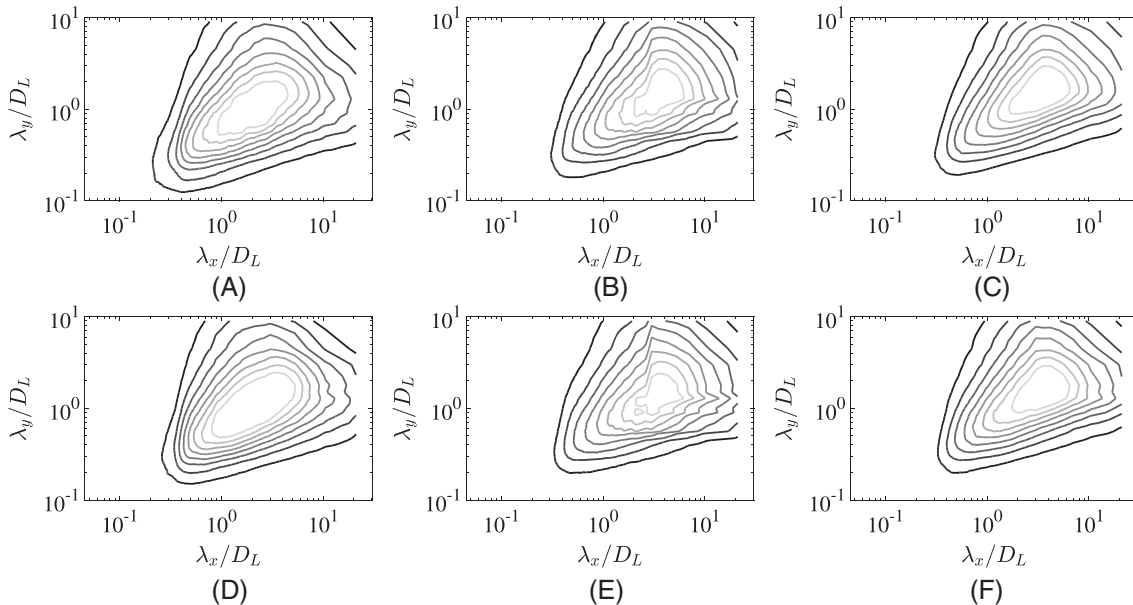


FIGURE 13 Two-dimensional premultiplied streamwise energy spectra $k_x k_y E_{uu} / U_\infty^2$ of the large turbines, top row: LI^M ; bottom row: L . A and D, $z = z_h - D_L/2$; B and E, $z = z_h$; and C and F, $z = z_h + D_L/2$. Contour levels: 10% to 80% of maximum, with the separation of 10% per each contour line; higher energy content is at lighter shades of grey

shifted towards smaller scales at $\lambda_x \approx D_L$, indicating towards an efficient harvesting of large-scale structures for power production via downdraft mechanisms in these wind farms.

It can be noted that some of the spectral lines in Figures 12 to 15 are not closed, due to the fact that some of these larger eddies that we capture, approach the size of the computational domain. These unclosed lines, however, pointing to the scales that are not captured, do not contaminate the scales that are captured. As an example, Del Alamo and coworkers,⁴² and later Loranzo-Durán and Jiménez,⁴³ by comparing the spectral information captured on two domain sizes, have shown that the smaller size of the domain acts by cutting off the information of the larger scales captured by a large domain, without significantly affecting the small/intermediate scale dynamics, in terms of shape, scaling laws, and anisotropy. That is, even if we do not capture the largest scales, the smaller scales that we do capture contain the correct information about their scaling laws and spatial coherence. Note that the most energetic eddies that contribute significantly to the energy captured by the wind turbines^{18,19,41} (of size $D = 10D$ and corresponding to 40% to 80% of maximum in Figures 12 to 15) are captured entirely, and the corresponding

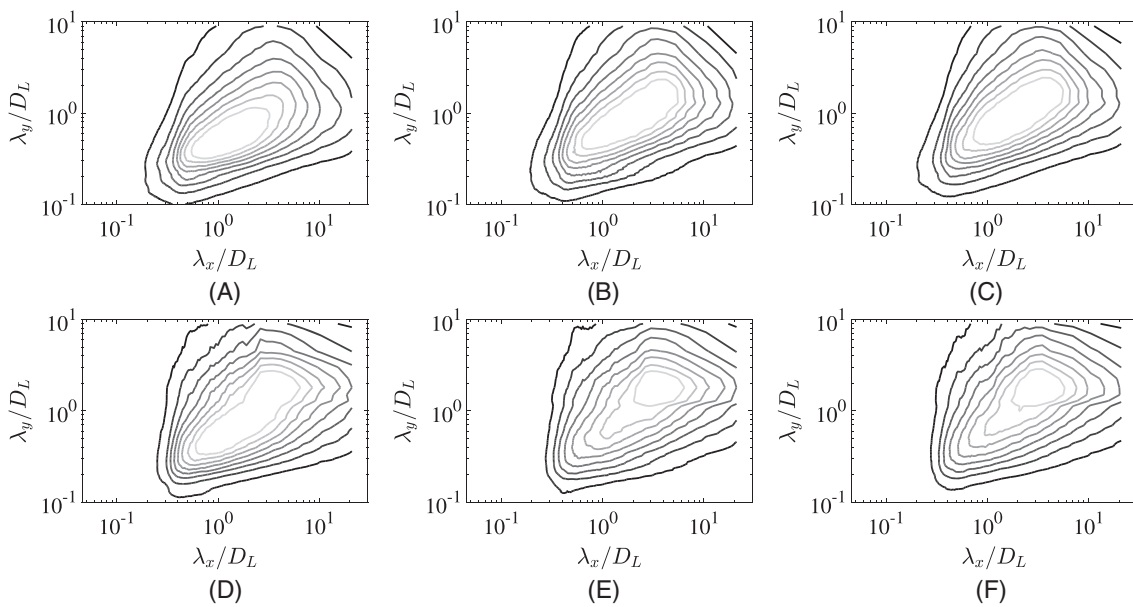


FIGURE 14 Two-dimensional premultiplied streamwise energy spectra $k_x k_y E_{uu} / U_\infty^2$ of the small turbines, top row: LS^M ; bottom row: S . A and D, $z = z'_h - D_s/2$; B and E, $z = z'_h$; C and F, $z = z'_h + D_s/2$. Contour levels: 10% to 80% of maximum, with the separation of 10% per each contour line, higher energy content is at lighter shades of grey

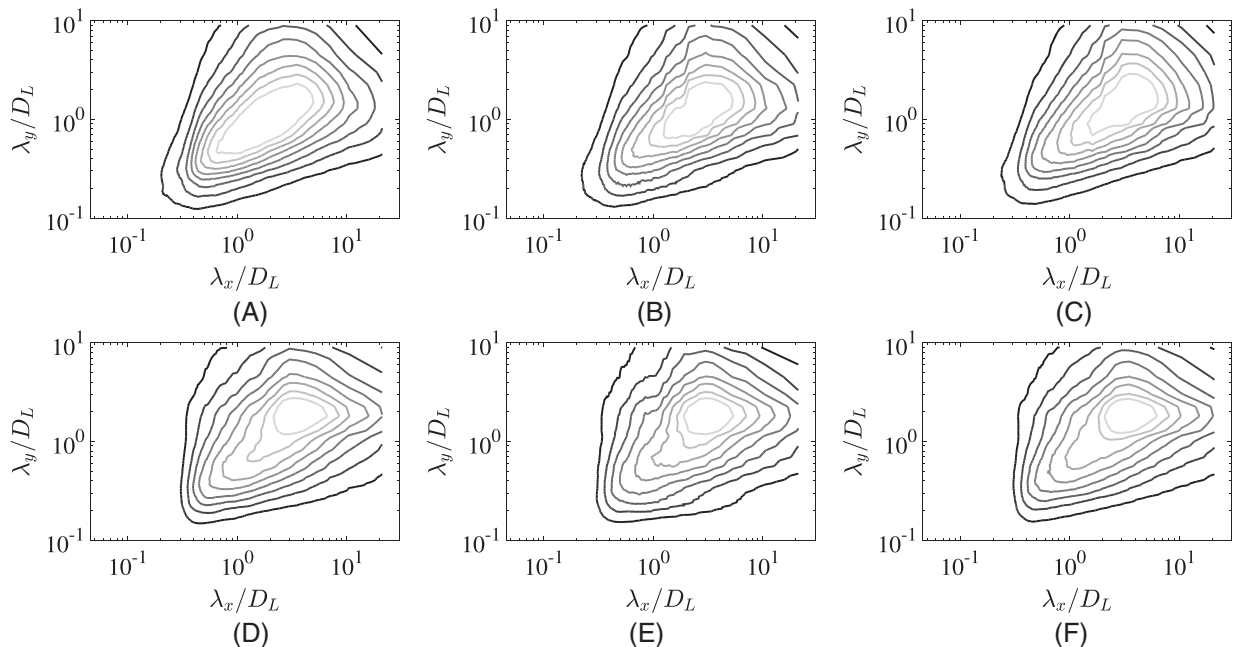


FIGURE 15 Two-dimensional premultiplied streamwise energy spectra $k_x k_y E_{uu} / U_\infty^2$ of the small turbines, top row: L^M ; bottom row: I . A and D, $z = z'_h - D_s/2$; B and E, $z = z'_h$. and C and F, $z = z'_h + D_s/2$. Contour levels: 10% to 80% of maximum, with the separation of 10% per each contour line, higher energy content is at lighter shades of grey

spectral lines for these scales are closed. Further increasing the domain size to capture the large-scale motions and their effect on wind turbine power would be an interesting study in the future; however, note that a fourfold to fivefold increase of the horizontal extent of the domain would be required to capture the large and very large scales of motion (LSM's & VLSM's) representative of turbulent boundary layers.⁴⁴

5 | DISCUSSION AND CONCLUSIONS

In the current study, we present large eddy simulations of a “multiscale” wind farm featuring HAWTs with two different rotor sizes and different hub heights in a vertically staggered arrangement. Two different multiscale arrangements were investigated: case LS^M with the small-size turbines located at hub heights of $0.3D_L$ and case L^M with the small-size turbines located at hub heights of $0.6D_L$; large turbines were kept fixed at

a hub height of D_L in both cases. In the explored configurations, it was found that the small/intermediate turbines had relatively small effect on large wind turbines mean power production. Although it was conjectured that the added small-size turbines had little contribution to the overall roughness of the farm land, they did increase the turbulent activity as evidenced by the increase in turbulent stresses, especially in the region corresponding to the bottom part of large turbine rotors, which resulted in a slight increase in power variability in large turbines due to an enhanced turbulence in the case L^M .

On the other hand, large turbines were found to affect the dynamics of the small/intermediate turbines significantly, both through the modulation of the inner region of the turbulent boundary layer via large-scale organized coherent motions in case LS^M , and through the direct interference and wake impingements in case L^M . In the presented configurations, a roughly 20% of power increase in the overall wind farms has been achieved for a one-to-one ratio of large to small/intermediate wind turbines in a collocated, vertically staggered arrangement (LS^M, L^M) compared with the baseline case L . In addition to an overall power increase, multiscale wind farms containing small wind turbines at hub height of $0.3D_L$ (case LS^M) demonstrated slightly better performance over the case L^M when compared against a linear sum of their respective single-scale counterparts, resulting from a more efficient operation of small turbines in multiscale arrays than in homogeneous arrays, and vice versa for intermediate turbines. The mechanisms responsible for the increased efficiency of small turbines in multiscale arrays were linked to an increased downdraft of kinetic energy to small turbines by the large-scale structures generated by the presence of large turbines. The evidence of these enhanced downdraft mechanisms were found in the increased levels of wall-normal turbulence fluctuations around small turbines, as well as in the 1D and 2D spectra of the turbulent kinetic energy. To the contrary, the intermediate wind turbines at hub heights of $0.6D_L$ were found to operate inefficiently and with increased power variability, possibly due to a direct inference of the large turbines on the small turbines through the mixing of wakes that alter the large-scale structure dynamics and suppress similar downdraft mechanisms. We note that the effects that wind turbine towers, both from large turbines and small/intermediate turbines, would have on the multiscale wind farm dynamics were not investigated in the current study.

The current study has two potential implications. First, it is instructive to explore whether the overall capacity of the multiscale wind farm in the current HAWT-only configuration can be further increased by increasing the density of the small turbines with respect to the large turbines. In the current study, the overall wind farm power production has increased with the addition of the smaller turbines by 20% in the large + small multiscale layout, and by 23% in the large + intermediate layout as can be seen from Table 7A. This number was calculated as the ratio of the total mean wind farm power in each multiscale case to the mean power observed in a “control” wind farm with large turbines only and does not take into account an increased cost associated with addition of more turbines into the wind farm. Note that these numbers are also representative of a specific wind and atmospheric stability conditions. In a recent study of Xie et al.¹⁵ the overall wind farm power production was found to increase by 32% in a combined HAWT-VAWT configuration (calculated in the same way as in the current study) with the ratio of the added small VAWT turbines to the large HAWT turbines of twenty to one. Since the small turbines in the current configuration are spaced nearly 23 and 10 diameters apart in streamwise/spanwise directions (scaled with the small turbines diameter), there is potentially room for increasing their density (which is currently kept at a one-to-one ratio) while still keeping an undesirable wake interference at a low level. This opens up an interesting possibility of optimizing such layouts, with respect to the density and streamwise location of small/intermediate turbines that might result in increased total power levels as well as an overall gain in multiscale wind farm power against the individual linear sum of powers attained in single-scale wind farms containing large and small/intermediate only turbines.

Second, the possibility of using large passive disked structures to modulate the flow around the turbines by generating bluff body wakes and organized coherent motions with a similar “shielding” effect would be of interest.

ACKNOWLEDGEMENTS

The authors T. Chatterjee and Y. Peet would like to gratefully acknowledge the support of NSF-CBET 13358568 grant and the computing hours of XSEDE Comet cluster as well as Penguin-on-Demand (POD) cluster made available by Arizona State University for the present work. T.C. and Y.P. also thank the anonymous reviewers whose comments have helped to significantly improve the manuscript. T.C. and Y.P. are not aware of any potential conflict of interest in this research.

ORCID

Tanmoy Chatterjee  <http://orcid.org/0000-0003-4992-5453>

REFERENCES

1. Ackermann T, Söder L. Wind energy technology and current status: a review. *Renewable Sustainable Energy Rev.* 2000;4:315-374.
2. Archer CL, Jacobson M. Evaluation of global wind power. *J Geophys Res Atmos.* 2005;110:905-921.
3. Stevens RJAM, Meneveau C. Flow structure and turbulence in wind farms. *Annu Rev Fluid Mech.* 2017;49:311-339.
4. Chamorro LP, Arndt REA, Sotiropoulos F. Turbulent flow properties around a staggered wind farm. *Boundary-Layer Meteorol.* 2011;141:349-367.
5. Meyers J, Meneveau C. Flow visualization using momentum and energy transport tubes and applications to turbulent flow in wind farms. *J Fluid Mech.* 2013;715:335-358.

6. VerHulst C, Meneveau C. Large eddy simulation study of the kinetic energy entrainment by energetic turbulent flow structures in large wind farms. *Phys Fluids*. 2014;8:025113.
7. Stevens RJAM, Gayme DF, Meneveau C. Effects of turbine spacing on the power output of extended wind-farms. *Wind Energy*. 2016;19:359-370.
8. Chamorro LP, Tobin N, Arndt REA, Sotiropoulos F. Variable-sized wind turbines are a possibility for wind farm optimization. *Wind Energy*. 2014;17:1483-1494.
9. Vested MH, Hamilton N, Sørensen JN, Cal RB. Wake interaction and power production of variable height model wind farms Journal of Physics: Conference Series 524 2014. The Science of Making Torque from Wind 2014 (TORQUE 2014).
10. Chen Y, Li H, Jin K, Song Q. Wind farm layout optimization using genetic algorithm with different hub height wind turbines. *Renew Energy*. 2013;70:56-65.
11. Chen K, Song M, Zhang X, Wang S. Wind turbine layout optimization with multiple hub height wind turbines using greedy algorithm. *Renew Energy*. 2016;96:676-686.
12. Wang L, Tan AC, Cholette M, Gu Y. Comparison of the effectiveness of analytical wake models for wind farm with constant and variable hub heights. *Energy Convers Manage*. 2016;124:189-202.
13. Jensen NO. A note on wind generator interaction Roskilde, Denmark: Riso National Laboratory; 1983.
14. Vasel-Be-Hagh A, Archer CL. Wind farm hub-height optimization. *Appl Energy*. 2017;195:905-921.
15. Xie S, Archer CL, Ghaisas N, Meneveau C. Benefits of collocating vertical-axis and horizontal-axis wind turbines in large wind farms. *Wind Energy*. 2017;20:45-62.
16. Dupont B, Cagan J, Moriarty P. An advanced modeling system for optimization of wind farm layout and wind turbine sizing using a multi-level extended pattern search algorithm. *Energy*. 2016;106:802-814.
17. Chatterjee T, Peet Y. Spectra and large eddy structures in the double log-layer in a high Re wind turbine array boundary layer. ASME Turbo Expo; 2016; Seoul, South Korea. <https://doi.org/GT2016-56359>
18. Chatterjee T, Peet Y. Contribution of large scale coherence to wind turbine power in a large eddy simulation model of periodic wind farms. *Phys Rev Fluids*. 2018;3:034601.
19. Chamorro LP, Lee SJ, Olsen D, Miliren C, Marr J, Arndt REA, Sotiropoulos F. Turbulence effects on a full-scale 2.5mw horizontal-axis wind turbine under neutrally stratified conditions. *Wind Energy*. 2015;18:339-349.
20. Fischer P. An overlapping Schwarz method for spectral element solution of the incompressible Navier-Stokes equations. *J Comp Phys*. 1997;133:84-101.
21. Chatterjee T, Peet YT. Regularization modelling for large-eddy simulation in wall-bounded turbulence: An explicit filtering-based approach. *Int J Numer Methods Fluids*. 2018;88(1):1-17.
22. Chatterjee T, Peet Y. Actuator line wind turbine simulations in atmospheric turbulent flows using spectral element method. AIAA paper 2015-2015-0727. 05 - 9 January 2015, Kissimmee, Florida.
23. Chatterjee T, Peet Y. Effect of artificial length scales in large eddy simulation of a neutral atmospheric boundary layer flow: A simple solution to log-layer mismatch. *Phys Fluids*. 2017;29:075105.
24. Troldborg N. Actuator line modeling of wind turbine wakes. Ph.D. Thesis: Technical University of Denmark; 2008.
25. Chatterjee T, Peet Y. Large eddy simulation of a 3 × 3 wind turbine array using actuator line model with spectral elements. AIAA paper 2016-1988 2016. 04 - 8 January 2016, San Diego, California.
26. Chatterjee T, Cherukuru NW, Peet Y, Calhoun R. Incorporating realistic geophysical effects of mean wind from lidar measurements in large eddy simulation of wind turbine arrays. AIAA paper 2017-1165 2017. 09 - 13 January 2017, Grapevine, Texas.
27. Ashill PR, Keating RFA. Calculation of tunnel wall interference from wall-pressure measurements. *Aeronaut J* (1968). 1988;92(911):3653.
28. Choi CK, Kwon DK. Wind tunnel blockage effects on aerodynamic behavior of bluff body. *Wind Struct*. 1998;1:351-364.
29. Chen TY, Liou LR. Blockage corrections in wind tunnel tests of small horizontal-axis wind turbines. *Exp Therm Fluid Sci*. 2011;35(3):565-569.
30. Sarlak H, Nishino T, Martinez-Tossas LA, Meneveau C, Sorensen JN. Assessment of blockage effects on the wake characteristics and power of wind turbines. *Renew Energy*. 2016;93:340-352.
31. Han Y, Stoellinger M, Naughton J. Large eddy simulation for atmospheric boundary layer flow over flat and complex terrains. *J Phys Conf Ser*. 2015;753:032044.
32. Allaerts D, Meyers J. Large eddy simulation of a large wind-turbine array in a conventionally neutral atmospheric boundary layer. *Phys Fluids*. 2015;27:065108.
33. Tjæreborg wind turbine (Esbjerg): Geometric and operational data Department of Fluid Mechanics, DTH, DK 2800, Lyngby VK-184; 1990.
34. Cushman-Roisin B. *Environmental Fluid Mechanics*. Hanover: John Wiley & Sons; 2013.
35. Gasch R, Twele J. Scaling wind turbines and rules of similarity. In: Gasch R, Twele J, eds. *Wind Power Plants: Fundamentals, Design, Construction and Operation*. Berlin, Heidelberg: Springer Berlin Heidelberg; 2012:257-271.
36. Churchfield MJ, Lee S, Moriarty PJ, Martinez LA, Leonardi S, Vijayakumar G, Brasseur JG. A large-eddy simulation of wind-plant aerodynamics AIAA Paper 2012-0537; 2012.
37. Troldborg N, Sørensen JN, Mikkelsen R. Numerical simulations of wake characteristics of a wind turbine in uniform inflow. *Wind Energy*. 2010;13:86-99.
38. Weihsing P, Schulz C, Lutz T, Krämer E. Comparison of the actuator line model with fully resolved simulations in complex environmental conditions. *J Phys Conf Ser*. 2017;854:012049.
39. Calaf M, Meneveau C, Meyers J. Large eddy simulation study of fully developed wind-turbine array boundary layers. *Phys Fluids*. 2010;22:015110.
40. Lettau H. Note on aerodynamic roughness-parameter estimation on the basis of roughness-element description. *J Appl Meteor*. 1969;8:828.
41. Hamilton N, Kang HS, Cal CMRB. Statistical analysis of kinetic energy entrainment in a model wind turbine array boundary layer. *J Renewable Sustainable Energy*. 2012;4:063105.
42. Álamo JD, Jiménez J, Zandonade P, Moser R. Scaling of the energy spectra of turbulent channels. *J Fluid Mech*. 2004;500:135-144.

43. Loranzo-Durán A, Jiménez J. Effect of the computational domain on direct simulations of turbulent channels up to $Re_\tau = 4200$. *Phys Fluids*. 2014;26:011702.
44. Balakumar BJ, Adrian RJ. Large and very-large-scale motions in channel and boundary-layer flows. *Phil Trans R Soc. 2007;365:665-681*.

How to cite this article: Chatterjee T, Peet Y. Exploring the benefits of vertically staggered wind farms: Understanding the power generation mechanisms of turbines operating at different scales. *Wind Energy*. 2019;22:283–301. <https://doi.org/10.1002/we.2284>